Cement and Concrete Research 39 (2009) 902–912

Contents lists available at ScienceDirect

Cement and Concrete Research

journal homepage: http://ees.elsevier.com/CEMCON/default.asp

Numerical and analytical effective elastic properties of degraded cement pastes

B. Bary [a,*], M. Ben Haha [a], E. Adam [b], P. Montarnal [c]

[a] CEA, DEN, DPC, SCCME, Laboratoire d'Etude du Comportement des Bétons et des Argiles, F-91191 Gif-sur-Yvette, France
[b] CEA, DEN, DM2S, SFME, Laboratoire de Génie Logiciel et de Simulation, F-91191 Gif-sur-Yvette, France
[c] CEA, DEN, DM2S, SFME, Laboratoire de Simulation des Ecoulements et du Transport, F-91191 Gif-sur-Yvette, France

ARTICLE INFO

Article history:
Received 23 January 2009
Accepted 11 June 2009

Keywords:
Elastic moduli
Numerical simulations
Cement paste
Homogenization
Degradation

ABSTRACT

Cement pastes are heterogeneous materials composed of hydrates, anhydrous products and pores of various shapes. They are generally characterized by a high particle concentration and phase contrasts, in particular in the case of degraded materials which exhibit important porosity. This paper compares the performance of several classical effective medium approximation schemes (Mori–Tanaka, Zheng-Du, self-consistent) through their ability to estimate the mechanical parameters of cement paste samples obtained numerically. For this purpose, finite element simulations are performed on 3D structures to compute for each sample accurate values of these mechanical properties. For these simulations, the cement paste is considered as a matrix of C–S–H in which are embedded inclusions of anhydrous, hydration products, and pores. In order to evaluate the importance of the particle shape, two types of samples are generated, one with only spherical inclusions and the other containing both spherical and prismatic particles. Simulations with three perpendicular loading directions and both uniform and mixed boundary conditions are performed in order to verify that the dispersion in the computed elastic moduli is low, or equivalently that the generated structures are close to representative volume elements (RVEs). It is shown that the considered effective medium approximation schemes, except the self-consistent one, provide relatively good estimations of the overall mechanical parameters when compared to simulation results, including when both particle volume fraction and phase contrast are high. The analytical methods taking into account the particle shapes also give estimates close to the corresponding numerical simulations, the latter confirming the influence of the particle form.

1. Introduction

The macroscopic properties of the composite materials depend mainly on the properties of the constitutive phases, their volume fraction, microgeometry and relative arrangement. The effects of the concentration and the shapes of inclusions on the physical properties of various compounds attracted the attention of researchers in many fields, in particular in materials science and mechanics. Analytical evaluations of the effective elastic properties of the composite can be obtained by several well-known methods. After the earliest work of Eshelby [1] on the stress field of an isolated ellipsoidal inclusion in an elastic infinite matrix, various schemes were developed to calculate the elastic properties of the composites of the matrix-inclusion type, as in the method of Mori–Tanaka (MT) [2,3] and self-consistent (SC) scheme [4–6]. They were based on the approximation of the mean-field, which supposes that the fields of stresses and strains in the matrix and in the inclusions are adequately represented by their volume fraction average, and differed from the way that they consider the elastic interaction between inclusions. Owing to the linearity condition, these average stresses or strains are directly related via fourth-order localization tensors to the macroscopic homogeneous stresses or strains. Obviously, these schemes converge when the volume fraction of particles or the contrast between the properties of the two phases is small, but the differences among them (and between upper and lower Hashin-Shtrikman bounds, [7]) may be very large otherwise. Their precision and extent of applicability may be established through analytical solutions (which do not exist in general for real materials due to their complex microgeometry) or by solving numerically the boundary value problem on a sample of the microstructure corresponding to a representative volume element of the composite. The characterization and definition of the RVE is essential in these numerical techniques. Indeed, the RVE has to contain a sufficiently important number of particles and heterogeneities to resemble cementitious materials, but must remain small enough to be considered as a volume element of continuum mechanics. Generally, the size of the RVE depends on the sought physical property, the contrast of properties between the different components, the volume fraction of the phases, and the number of microstructure realizations and the precision of the wanted estimation of macroscopic properties [8,9]. Another alternative method for obtaining numerical estimations of these elastic properties consists to

* Corresponding author.
E-mail address: benoit.bary@cea.fr (B. Bary).

0008-8846/$ – see front matter © 2009 Elsevier Ltd. All rights reserved.
doi:10.1016/j.cemconres.2009.06.012

generate structures smaller than the RVE, which requires in general excessive computations, and to balance by calculating the average apparent properties on several realizations [8]. Interestingly, previous studies have reported that a RVE size of about two times the dimension of the heterogeneities (reinforcements) allows to obtain estimates of these properties for a two-phase material with an error of the order of 5%, whereas a RVE over heterogeneities ratio of 5 provides predictions as close as 1%, whatever the inclusion concentration and phase contrast [10,11]. In contrast, the 2D results of Pecullan et al. tend rather to show that for high properties contrasts, a ratio between the RVE size and the particle of 6 still leads to important variations of apparent moduli obtained with uniform displacement (Dirichlet) and stress (Neumann) boundary conditions [9].

The boundary value problem is in general solved numerically by means of the finite element (FE) method, and the precision and adequateness of the numerical model rely then mainly on the microstructure geometry and the quality of the mesh produced. Several methods allow generating the geometry of cement pastes numerically. Some of them are based on hydration models providing more or less complex microstructures generally composed of elementary particles of spherical shape whose size is not necessarily limited (e.g. [12]), and possibly discretized by means of cubic pixels (e.g. [13]). Others result from a random distribution of inclusions representing hydrated products with predefined size and shape, the latter being usually spherical as it greatly simplifies the generation process (e.g. [14]). The second difficulty of numerical calculations concerns the creation of the 3D meshes from the generated microgeometry. Indeed since the structure involves numerous inclusions with physical properties different from the ones of the matrix, the application of the classical finite element method requires each inclusion to be meshed independently. The resulting mesh may then contain a huge number of elements and nodes, especially when the size ratio and distance between particles are high and low, respectively. When conformant mesh are generated, the meshing algorithm has further to be efficient, in particular for performing the surface elements; in contrast, when space is discretized by means for instance of cubic pixels, the meshing effort is greatly reduced (see e.g. [14,15]). To overcome these meshing difficulties, a promising way lies in the recourse of extended finite element techniques (XFEM) combined with level set method (see e.g. [16,17]).

In this paper, we propose to investigate the precision of some of the more widely used effective medium approximation schemes (MT, SC and Interaction Direct Derivative (IDD) schemes) by comparing them to numerical simulations. For this purpose, 3D cement paste samples were generated with the hypothesis that this material may be viewed as a C–S–H matrix in which are distributed inclusions of other main hydrated products, remaining anhydrous components and capillary pores. This type of morphology is commonly observed in classical hydrated CEM I cement pastes (e.g., [18]), while it is questionable in the early phases of hydration when a continuous matrix has not yet formed. Specific morphologies ideally issued from hydration codes should then be used in this case. The volume fractions of the different phases were determined experimentally by image analysis techniques. The obtained numerical structures were then meshed and finite element simulations were performed so as to gain the macroscopic mechanical parameters. The validity of these structures to be considered as RVE is assessed by comparing the results obtained when the three perpendicular directions are alternately loaded, and when different uniform and mixed boundary conditions are applied. Several degradation scenarios of the material were considered. We then assumed that the main hydrated products were either present or totally dissolved, and that the C–S–H could have reduced mechanical properties consecutive to a severe leaching process. In order to evaluate the influence of the particle shape, samples were generated with a part of inclusions being prismatic (to mimic elongated shapes as may be encountered in the case of well-crystallized ettringite, and flat hexagonal shapes representing well-crystallized portlandite). The simulations confirmed that this shape is influential, as already reported in many studies (e.g. [19,20]). The corresponding effects appeared to be quite well captured by the approximation schemes, which are capable to take into account ellipsoidal particle shapes. Overall, except for the SC method, numerical and analytical results were found to be relatively close in the case of the displacement-imposed mixed boundary conditions, even in the case of an important pore volume fraction (up to 35%) consecutive to a totally degraded material and an infinite property contrast ratio between matrix and inclusion phases.

2. Analytical models

In this section we briefly recall the main formulae leading to the estimations of the effective medium approximation schemes retained in this study. The following widely used schemes are considered in the isotropic case: the MT method ([2]), the SC scheme and the IDD scheme due to [21]. The representative volume element with total volume V of the material consists of $n+1$ phases that fill homogeneous regions within the material, and which have different properties and are separated from each other with well-defined interfaces. The matrix phase is labelled by 0 and r designates the particulate phases; ε_r is the strain tensor in phase r and σ_r is the stress tensor. The volume averages of strain and stress within phase r are classically defined as follows:

$$\bar{\varepsilon}_r = \frac{1}{V_r}\int_{V_r}\varepsilon_r dV,\ \bar{\sigma}_r = \frac{1}{V_r}\int_{V_r}\sigma_r dV \tag{1}$$

where V_r is the volume occupied by phase r. Likewise, the overall average strain and stress are expressed as:

$$\bar{\varepsilon} = \sum_{r=0}^{n}\phi_r\,\bar{\varepsilon}_r,\ \bar{\sigma} = \sum_{r=0}^{n}\phi_r\,\bar{\sigma}_r = \sum_{r=0}^{n}\phi_r\,\boldsymbol{C}_r\,\bar{\varepsilon}_r \tag{2}$$

with $\phi_r = V_r/V$ and $\boldsymbol{C}_r$ being the volume fraction and the elasticity tensor of phase r, respectively. The overall elasticity tensor $\boldsymbol{C}$ is further classically defined such that $\bar{\sigma} = \boldsymbol{C}\bar{\varepsilon}$. The schemes to determine $\boldsymbol{C}$ are obtained by assuming that a macrostrain ε_0 is imposed, leading to $\bar{\varepsilon} = \varepsilon_0$. Thus, thanks to the linearity the problem is equivalent to finding the way to express $\bar{\varepsilon}_r$ in terms of ε_0 through $\bar{\varepsilon}_r = \boldsymbol{A}_r\varepsilon_0$, where $\boldsymbol{A}_r$ is the localisation tensor. The latter is determined by using the eigenstrain approach, in which the Eshelby's equivalent inclusion theory is used and the Eshelby tensor is therefore required. Over the last three decades, a large number of micromechanics models have been developed to predict the overall elastic properties of heterogeneous materials and their dependence on materials microstructure. Most of these models are based on the Eshelby's equivalent inclusion method (see e.g. [22]).

We now briefly recall the main expressions of the effective medium approximation methods considered here. The IDD scheme is based on the following relation [21]:

$$\boldsymbol{H}^{\mathrm{IDD}} = \left[\boldsymbol{I} - \sum_{i=1}^{n}\boldsymbol{H}_i^d\boldsymbol{\Omega}_{D_i}^0\right]^{-1}\boldsymbol{H}^d \tag{3}$$

where $\boldsymbol{H} = \boldsymbol{S} - \boldsymbol{S}_0$ and $\boldsymbol{H}_r = \boldsymbol{S}_r - \boldsymbol{S}_0$ designate the compliance increment and compliance fluctuations, respectively, with $\boldsymbol{S}_r = \boldsymbol{C}_r^{-1}$ and $\boldsymbol{S} = \boldsymbol{C}^{-1}$ the compliance tensors of phase r and of the effective medium; $\boldsymbol{I}$ denotes the fourth-order identity tensor. In Eq. (3), the dilute estimate for the compliance increment $\boldsymbol{H}^d$ and the dilute estimate of type-i inclusion $\boldsymbol{H}_i^d$ are defined as:

$$\boldsymbol{H}^d = \sum_{i=1}^{n}\boldsymbol{H}_i^d,\ \boldsymbol{H}_i^d = \phi_i(\boldsymbol{H}_i^{-1} + \boldsymbol{\Omega}_i^0)^{-1} \tag{4}$$

where the eigenstiffness tensor $\boldsymbol{\Omega}_i^0 = \boldsymbol{C}_0(\boldsymbol{I}-\boldsymbol{\Sigma}_i^0)$, with $\boldsymbol{\Sigma}_i^0$ denoting the Eshelby tensor of the inclusion ω_i embedded in the matrix. One of the main characteristic of the IDD scheme is that it takes into account explicitly the distribution of the inclusions ω_i through the tensor $\boldsymbol{\Omega}_{D_i}^0$. The latter defines the geometry of the cell ω_i^D of matrix material surrounding each inclusion, such that the union of ω_i and its matrix atmosphere should be representative of the real distribution of the particulate phase [21]. In the sequel, the geometry of the cell is limited to ellipsoidal shapes for simplicity. Note that for randomly distributed inclusions as necessarily considered in this study to comply with the isotropy condition, all summed quantities in Eqs. (3) and (4) should be replaced by their average counterparts, i.e. $\boldsymbol{H}_i^d\boldsymbol{\Omega}_{Di}^0$ and $\boldsymbol{\Omega}_i^0$ become $\{\boldsymbol{H}_i^d\boldsymbol{\Omega}_{Di}^0\}$ and $\{\boldsymbol{\Omega}_i^0\}$, respectively, the curly brackets designating the average operation over all possible orientations. Connections with the Ponte Castañeda–Willis (PCW) method [23] and with the MT scheme are established in [21]. For example, PCW and IDD estimates are shown to coincide providing that correlation functions of all inclusion pairs in the PCW model have the same ellipsoidal distribution characterized by the same eigenstiffness tensor $\boldsymbol{\Omega}_D^0$ for all inclusions in the IDD scheme.

It may be shown that in the isotropic case (for randomly oriented and distributed particles), Eq (4) reduces to the following expressions for the mechanical parameters [20,24]:

$$k^{\mathrm{IDD}} = k_0\left(1+\frac{\sum_i \phi_i T_i^h(1-k_i/k_0)}{1-\sum_i \phi_i(\Xi_i^h - T_i^h k_i/k_0)}\right)^{-1},$$

$$\mu^{\mathrm{IDD}} = \mu_0\left(1+\frac{\sum_i \phi_i T_i^d(1-\mu_i/\mu_0)}{1-\sum_i \phi_i(\Xi_i^d - T_i^d \mu_i/\mu_0)}\right)^{-1} \tag{5}$$

where T_i^h and T_i^d are the hydrostatic and deviatoric parts, respectively, of the averaged dilute strain localization tensor $\{\boldsymbol{T}_i^0\}$ defined by:

$$\{T_i^0\} = \{(I-\Sigma_i^0(I-\mathbf{C}_i\mathbf{C}_0^{-1}))^{-1}\} = T_i^h\boldsymbol{L} + T_i^d\boldsymbol{J} \tag{6}$$

with $\boldsymbol{L}$ and $\boldsymbol{J}$ the classical projection operators such that $\boldsymbol{L} = \frac{1}{3}1\otimes 1$ and $\boldsymbol{J} = 1\overline{\otimes}1-\boldsymbol{L}$, 1 being the second order identity tensor (i.e. $L_{ijkl} = \frac{1}{3}\delta_{ij}\delta_{kl}$ and $J_{ijkl} = \frac{1}{2}(\delta_{ik}\delta_{jl}+\delta_{il}\delta_{jk}) - \frac{1}{3}\delta_{ij}\delta_{kl}$, with δ the Kronecker delta); Ξ_i^h and Ξ_i^d are also the hydrostatic and deviatoric components of the isotropic tensor $\Xi_i = \{\boldsymbol{T}_i^0(\boldsymbol{T}_{Di}^0)^{-1}\}$, with $\boldsymbol{T}_{Di}^0 = (\boldsymbol{I}-\boldsymbol{\Sigma}_{Di}^0)^{-1}$; k and μ designate the bulk and shear moduli, respectively. In the applications shown in the next sections, the performance of the schemes will be assessed by comparison with FE simulations of structures in which are dispersed spherical as well as non-spherical inclusions. Since simple and exact evaluation of Eq. (6) is only achievable for ellipsoidal particle shapes, we limit ourselves to such shapes from now on. The main difficulty to apply the considered approximation methods then lies in the calculation of the quantities T_i^h, T_i^d, Ξ_i^h and Ξ_i^d, which are related to both inclusion and surrounding cell shapes through the Eshelby tensors $\boldsymbol{\Sigma}_i^0$ and $\boldsymbol{\Sigma}_{Di}^0$, respectively. Because the latter are well described elsewhere (see e.g. [22,25]), they are not recalled here.

Note that in the case where the i-type inclusions and their surrounding cell are identical in both shape and orientation, then $\Xi_i^h = \Xi_i^d = 1$ and Eq. (5) becomes analogous to the MT scheme as proposed by [2]; Eq. (5) reduces to:

$$k^{\mathrm{MT}} = k_0\left(1+\frac{\sum_i \phi_i T_i^h(1-k_i/k_0)}{\phi_0+\sum_i \phi_i T_i^h k_i/k_0}\right)^{-1},$$

$$\mu^{\mathrm{MT}} = \mu_0\left(1+\frac{\sum_i \phi_i T_i^d(1-\mu_i/\mu_0)}{\phi_0+\sum_i \phi_i T_i^d \mu_i/\mu_0}\right)^{-1} \tag{7}$$

Moreover, for spherical inclusions randomly distributed MT, IDD and PCW estimates coincide and the overall bulk and shear moduli take the following form (e.g., [22]):

$$\frac{k-k_0}{k+4/3\mu_0} = \sum_{r=1}^{n}\phi_r\frac{k_r-k_0}{k_r+4/3\mu_0},\quad \frac{\mu-\mu_0}{\mu+H_0} = \sum_{r=1}^{n}\phi_r\frac{\mu_r-\mu_0}{\mu_r+H_0},$$

$$\text{with } H_r = \frac{\mu_r(3/2k_r+4/3\mu_r)}{k_r+2\mu_r} \tag{8}$$

The SC estimate for the effective elastic moduli was originally proposed by Hill [6] and Budiansky [26], based on previous developments by [4] and [5] (see e.g. [22]). It consists in assuming that perturbations due to each type of inclusion be zero on average. Then in the isotropic case (i.e. for randomly oriented particles) the effective elastic parameters k^{SC} and μ^{SC} are obtained by solving the following implicit equations [22]:

$$\sum_{i=0}^{n}\phi_i T_i^{SC,h}(k_i-k^{SC}) = 0,\ \sum_{i=0}^{n}\phi_i T_i^{SC,d}(\mu_i-\mu^{SC}) = 0 \tag{9}$$

where $T_i^{SC,h}$ and $T_i^{SC,d}$ are the hydrostatic and deviatoric parts of the averaged dilute strain localisation tensor as defined in Eq. (6), but referred to the yet unknown effective material, i.e. $\{\boldsymbol{T}_i^{SC}\} = \{(\boldsymbol{I}-\boldsymbol{\Sigma}_i^{SC}(\boldsymbol{I}-\boldsymbol{C}_i\boldsymbol{C}_{SC}^{-1}))^{-1}\}$. In the case of spherical inclusions, the previous expressions simplify as:

$$\sum_{i=0}^{n}\phi_i\frac{k_i-k^{SC}}{k_i+4/3\mu^{SC}} = 0,\ \sum_{i=0}^{n}\phi_i\frac{\mu_i-\mu^{SC}}{\mu_i+H_{SC}} = 0,$$

$$\text{with } H_{SC} = \frac{\mu^{SC}(3/2k^{SC}+4/3\mu^{SC})}{k^{SC}+2\mu^{SC}} \tag{10}$$

3. Numerical models

The methodology adopted to create the 3D heterogeneous structures and to perform the FE simulations is described in this section. In the first subsection are explained the way the 3D meshes representing simplified hydrated cement pastes are generated. The second subsection presents the results obtained; the issues relative to the validity of the hypothesis of representative element volume are further examined through additional simulations.

3.1. Generation of 3D models

As already mentioned, cement pastes are viewed here as a composite material formed of a C–S–H matrix in which are distributed particles of other hydrated products (portlandite, ettringite), anhydrous residuals and pores. In the numerical homogenization technique, the common approach to model the macroscopic properties of composites of the matrix-inclusion type, and thus cement pastes, is to create the RVE that should capture the major features of the underlying microstructure. The precision and adequacy of this method depend then largely upon the generation of a globally homogeneous medium equivalent to the original composite, where the strain energy stored in both systems is approximately the same. The methodology and the numerical tool which are proposed in this work enable an efficient and precise evaluation of the analytical homogenisation schemes, and minimize the problems concerning the size and the ratio of the inclusions used, and the minimal distance between inclusions (as encountered in the case for instance of voxel-type approaches). However, in order to restrict the computational time, only a limited number of inclusions (between 850 and 2800) will be used. Because of this practical restriction, the proposed methodology cannot evaluate exhaustively all situations. In particular, the pore phase will only consist in capillary pores regarded as separate inclusions. The gel pores are consequently assumed to be integrated in the C–S–H phase. This is equivalent to considering the

Table 1
Chemical composition of hydrated cement paste used for this study (unit volume fraction from total content).

Phases	Fraction content
C–S–H + other hydrates	0.652
CH, monosulfate, monocarbonate	0.177
Anhydrous phase	0.093
Capillary porosity	0.078

resulting heterogeneous material at the microscale (the particles have a size of the order of micrometer).

The maximum ratio of inclusions size is approximately 6. The inclusion volume fraction is kept constant for these simulations and investigations of the influence of property contrast, inclusions shape and porosity level are performed through the examination of several degradation states of the material. We have then considered the following configurations for the material: intact (i), without portlandite (p), without portlandite and with degraded mechanical properties for the C–S–H phase (d), and the same as (d) without anhydrous residuals (td). Theses configurations correspond classically to simplified decalcified states for the cement pastes. In order to study the effects of the particle shape, two types of RVE have been generated, one with only spherical inclusions and the other including prismatic particles. The latter shapes are chosen to approach in a very simplified manner needle-like components (typically ettringite) and hexagonal platelets (which mimic well-crystallised portlandite).

A software generating automatically samples constituted of the matrix containing a given volume fraction of inclusions randomly distributed in a finished volume has been used. This program is developed in python language and makes use of the geometry module of the integration platform for numerical simulations Salome [27]. This module provides a list of functions for working with computer-aided design (CAD) models and can correct them to be consistent with meshing algorithms. All inclusions are spatially non-correlated, which means that the spatial position of grains is truly random. Consequently, particular aspects like the influence of packing density and heterogeneity in packing density may not be analyzed with the module in its current version. As the minimal distance between particles may be calculated with high accuracy whatever their shape via Salome functionalities, their placement may be set very precisely. No particular treatment of the RVE boundaries is performed regarding the inclusions position; the latter may then intersect randomly these boundaries (i.e. no periodic particle arrangement is imposed).

In the examples presented below, the maximal dimension of particles is limited to 5 times lower than the dimension of the box edge forming the RVE. The bigger inclusions are constituted of anhydrous residuals, followed by the hydrated products and then by porosity. The size of the smallest particles is about 30 times lower than the RVE characteristic dimension. The size of the inclusions for each family (in practice, each phase constitutes a family) is allowed to vary by a ratio ranging from 0.5 to 1.3 from a reference value set by the user, in order to get particle distributions resembling more to real microstructure and also to accelerate the placement process. The RVE is chosen to be a cube with dimensions $100\times 100\times 100\ \mu m^3$. It is to be noticed that the unit adopted (μm) is only indicative since the particles size is not precisely correlated with real ones (through image analysis technique for instance). The minimal distance between inclusions is set to 0.3 μm. They are then not allowed to be in contact, this restriction being essentially dictated by computational costs since particle contact or overlapping pose no particular difficulty from the geometry process point of view. Besides, we are not interested here in studying phase percolation properties, which is by contrast essential when addressing diffusivity problems.

Typical cement was chosen and the amounts of principal hydrates, anhydrous residuals and porosity have been measured by means of SEM-image analysis (see e.g. [28]). The results of the chemical composition given by this analysis are listed in Table 1. It is noteworthy that in this material ettringite was not detected, although some small ettringite particles may be intricately dispersed in the C–S–H phase. The resulting 3D particle distributions are shown on Fig. 1 for the two configurations: spherical inclusions (a) and both spherical and prismatic inclusions (b). The number of particles is approximately 850 and 1800 for these two cases, respectively. The second configuration contains more particles due to the greater difficulty to achieve the same packing in the case of non-spherical inclusions. Indeed, for a given maximum dimension, the sphere is the geometry which maximizes the corresponding particle volume. The prismatic inclusions used in configuration (b) are depicted in Fig. 2. Two types of elongated particles are introduced, which differ by their size and number of lateral faces (6 and 8). The aspect ratios defined by the maximal dimension of the basis (surface normal to the lateral faces) over the particle height are set to 3 and 4 for the elongated and platelet-like particles, respectively. The distributions for each of these

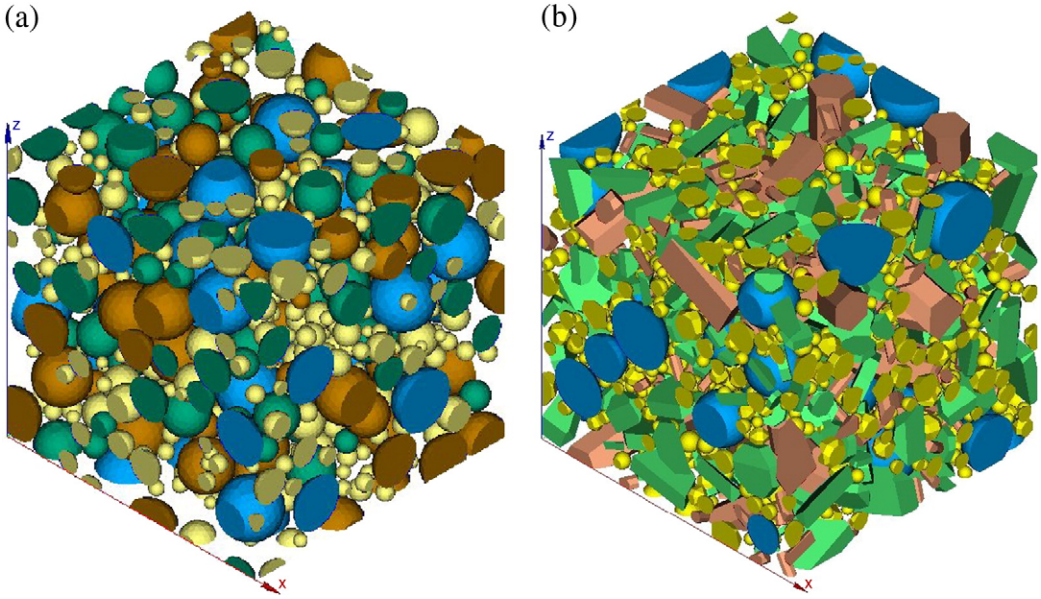

Fig. 1. Particle distributions for the two considered cases: spherical inclusions (a), and mix of spherical and prismatic inclusions (b).

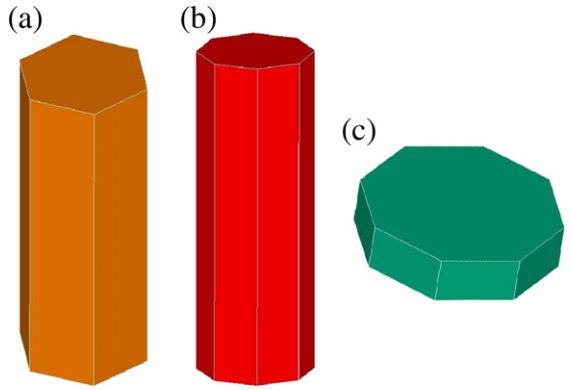

Fig. 2. Prismatic particles used in the configuration (b) of Fig. 1: elongated with 6 faces (a) and 8 faces (b), platelet-like with 8 faces (c).

inclusion families are detailed in Fig. 3(a) and (b) for the reference geometry; pores are also represented in Fig. 3(c). Note that the microstructure with non-spherical shapes is more difficult to compute and requires much more CPU time than with only spherical ones since the placement process requires for the former case to work out explicitly using Salome functionalities numerous distances between randomly oriented quite complex shapes, whereas for the spherical case these quantities are immediately known from the inclusion centres.

3.2. Meshing and FE simulations

Once the geometry of the structure is performed, a mesh can be generated via Salome. We used the automatic meshing softwares BLSURF and GHS3D developed by Distene to compute the surface meshes and the volume ones. BLSURF is a mesh generator for surfaces composed of parametric patches, conforming to a prescribed size map. GHS3D is a meshing software component which creates automatically tetrahedral meshes out of closed triangular surface meshes. For the examples presented here, it takes about 15 to 20 mn to create the entire meshes with a standard 8 GB-RAM PC Linux. The number of volume elements generated is about 2.5×10^6 and 4×10^6 for the

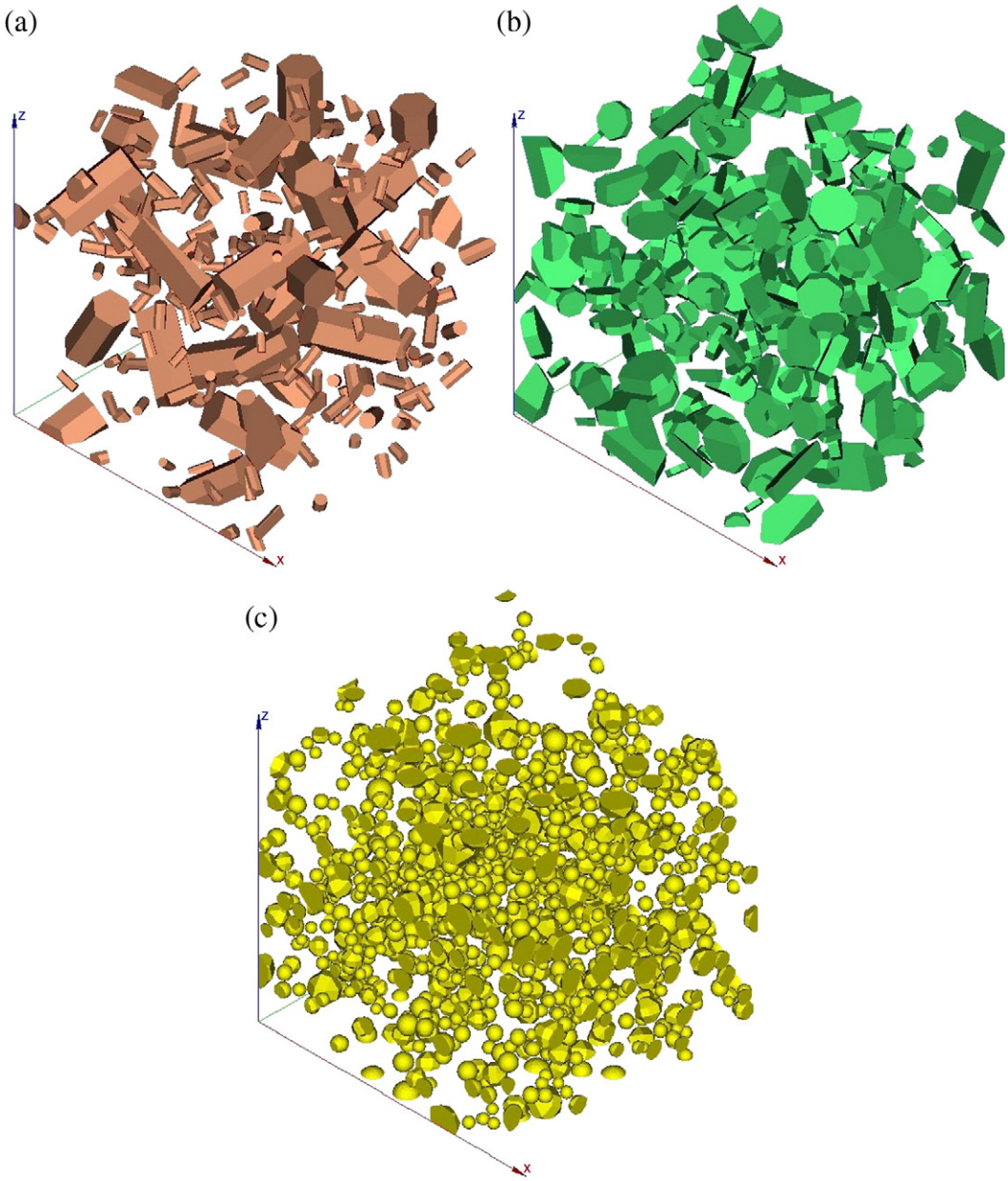

Fig. 3. Prismatic elongated (a), prismatic platelet-like (b) and pore inclusions (c) for the 3D microstructure of Fig. 1 (b).

spherical particle and non-spherical particle microstructures, respectively, and the corresponding number of nodes is approximately 6×10^5 and 7.5×10^5.

To get the macroscopic properties of the generated numerical samples of the microstructure, conditions must be prescribed on their boundaries. For this purpose, the most classical boundary conditions are the kinematic uniform and static uniform ones (Dirichlet and Neumann, respectively). They are defined by the displacement $\boldsymbol{u}$ and the traction vector $\boldsymbol{t}$, respectively, imposed at each point $\boldsymbol{x}$ of the boundary ∂V such that:

$$\boldsymbol{u} = \boldsymbol{E}.\boldsymbol{x}(\text{kinematic}),\ \boldsymbol{t}.\boldsymbol{n} = \boldsymbol{\Sigma}.\boldsymbol{n}(\text{static}),\ \forall \boldsymbol{x}\in\partial V \tag{11}$$

with $\boldsymbol{E}$ and $\boldsymbol{\Sigma}$ two macroscopic strain and stress tensors, respectively, independent of $\boldsymbol{x}$, and $\boldsymbol{n}$ designates the vector normal to ∂V at $\boldsymbol{x}$. These two types of boundary conditions lead to the computations of two apparent elastic properties of the material associated with the volume of the sample V and involved in the stiffness tensor $\boldsymbol{C}_E$ and the compliance tensor $\boldsymbol{S}_\Sigma$, respectively, which are in general different. When the RVE size is sufficiently large (i.e. V is great), then the elastic properties do not depend on the boundary conditions and necessarily $\boldsymbol{C}_E = \boldsymbol{S}_\Sigma^{-1} = \boldsymbol{C}^{eff}$, with $\boldsymbol{C}^{eff}$ containing the sought effective moduli of the heterogeneous material [29]. For a volume V smaller than the RVE, the following inequalities hold [30,31]:

$$\boldsymbol{S}_\Sigma^{-1} \le \boldsymbol{C}^{eff} \le \boldsymbol{C}_E \tag{12}$$

These inequalities must be understood in the sense of quadratic forms. In the case where the sample volume is smaller than the RVE one (or to simplify the simulation process), it may be interesting to mix the boundary conditions since the computed elastic moduli always lie between $\boldsymbol{S}_\Sigma^{-1}$ and $\boldsymbol{C}_E$. In this study, in addition to the classical kinematic and static uniform boundary conditions defined in Eq. (11), two types of mixed boundary conditions are imposed on the cubic RVE faces. The first one consists in prescribing homogeneous displacements on the cube faces. Two kinds of such loadings are used. To get the bulk modulus, we propose to prescribe zero displacement on a particular face and at the same time on the four faces in contact with it, in the direction perpendicular to each of these faces, and then to impose a displacement on the opposite face (see Fig. 4 left). In that case the macroscopic bulk strain is simply given by this imposed displacement divided by the dimension of the face edge. For the shear modulus, a second loading in which the displacements are imposed parallel to the face located at the opposite side of the blocked one, as depicted on Fig. 4 right, is prescribed. Note that these loadings constitute mixed boundary conditions since the displacements are prescribed in only one direction per face (normal to this face for the bulk modulus, both normal and parallel for the shear modulus). Consequently in the two other directions of each face the loading is similar to stress-imposed conditions set to zero (i.e. the displacements result from the FE computations). In the following the latter loadings will be referred to as displacement-imposed mixed boundary conditions. The second type of mixed boundary conditions is similar to the previous one except that forces resulting from the action of a homogeneous pressure are imposed on each node of the loaded face (large arrows on Fig. 4) instead of displacements. Then the influence of mixed displacement-imposed boundary conditions and stress-imposed ones may be evaluated on the considered structures with regard to both static and kinematic uniform boundary conditions. In addition, for each degraded configuration of the material as defined above (that is, from intact to totally decalcified material) and for both elastic parameters, three numerical simulations are carried out by considering different perpendicular directions (and then different faces) for the imposed displacements or forces. Thus, the validity of the generated heterogeneous microstructures to be considered as approximate RVEs may be partly assessed through the comparison of the results in the three directions.

Table 2
Elastic moduli of individual cement paste phases.

Minerals of cement paste	k (GPa)	μ (GPa)	Reference
C3S, C2S, C4AF, C3A (anhydrous phases)	105.2	44.8	[32]
CH, monosulfate, monocarbonate	40	16	[32]
C–S–H, hydrogarnet, ettringite, iron hydroxide,	14.93	8.96	[32]
Decalcified C–S–H	2.756	1.734	[33]

The simulations are performed with the finite element code Cast3m developed at CEA. An iterative procedure is used to solve the linear system; it takes between 3 and 20 h to achieve the solution on a 16 GB PC Linux (3 GHz), depending on both computed structures and boundary conditions. Indeed, in the case of the totally decalcified material the problem to solve is much smaller than for the intact one in which both portlandite and anhydrous phases (and then the corresponding meshed regions) are present. Moreover, in the case of Dirichlet boundary conditions the number of unknowns is lower than for Neumann boundary conditions since all nodes at the surfaces of the sample have prescribed displacements in the former case. Then the time computation is slightly bigger in the case of Neuman boundary conditions due to the higher number of unknowns. The elastic parameters of the elementary phases used for the simulations are listed in Table 2.

The results obtained in terms of overall bulk and shear moduli averaged over the three loading directions are shown on Fig. 5 in the case of both kinematic a) and static b) uniform boundary conditions. These results are depicted as a function of the (capillary) porosity varying with the degradation states considered in this study. As expected, from Fig. 5 it is clear that the inclusions shape influences the results, in particular for the bulk modulus and for degraded material, in such a manner that needle-shaped and disk-shaped inclusions have more impact on macroscopic properties than their spherical counterparts (i.e. they tend to further decrease the effective properties than spherical shapes in the case of void inclusions). The differences are more marked in the case of static uniform boundary conditions and attain 26% for the bulk modulus and 14% for the shear modulus for all degraded configurations. In contrast, the elastic parameters for the non-degraded material are very close for the cases with spherical and

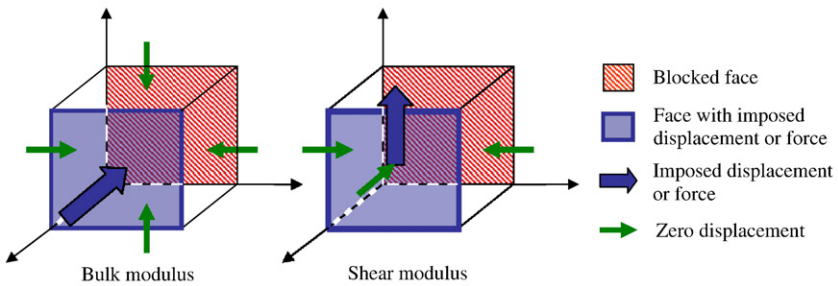

Fig. 4. Schematic representation of the mixed boundary conditions prescribed on the RVE faces.

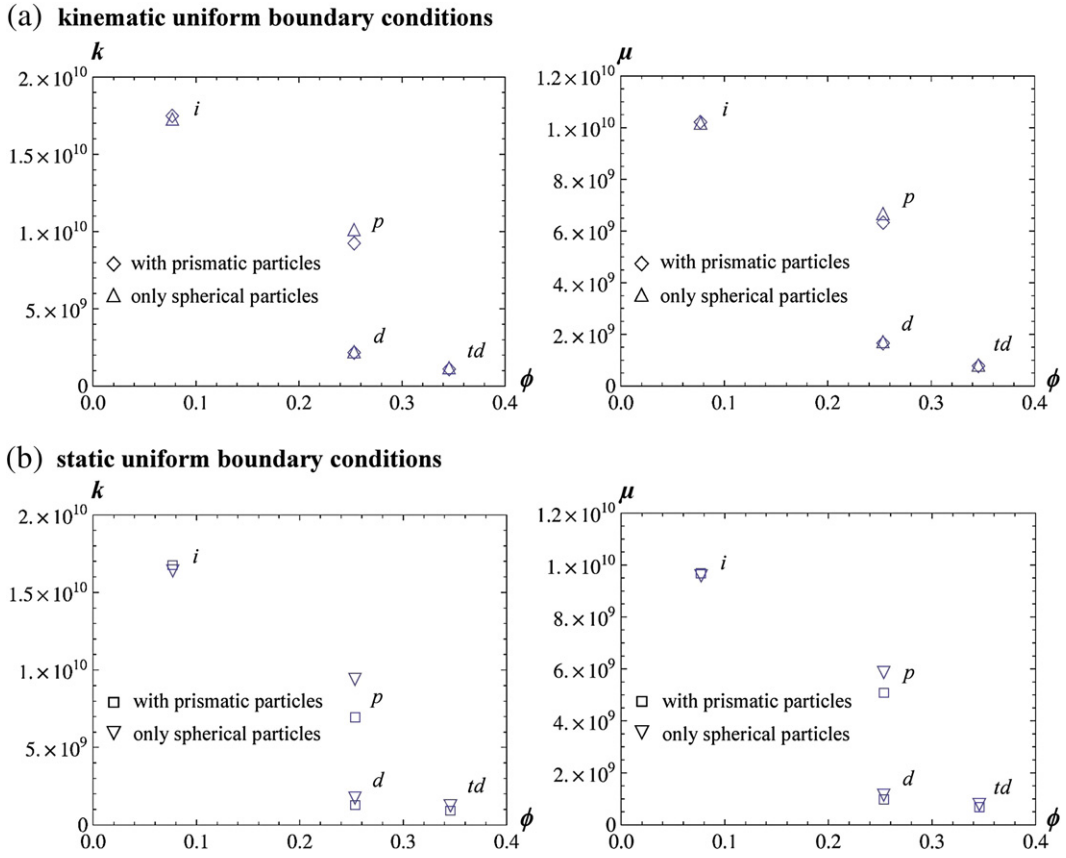

Fig. 5. FE average effective parameters for the microstructures containing only spherical particles and a mix of prismatic and spherical ones, as a function of the porosity corresponding to the considered degraded states (intact (i), without portlandite (p), same as (p) with degraded C–S–H (d), same as (d) without anhydrous residuals (td)), and for kinematic a) and static b) uniform boundary conditions.

non-spherical particles (variations less than 2%). This is probably due to the fact that the intact material contains inclusions whose phases are stiffer (portlandite, anhydrous residuals) as well as more compliant (porosity) than the matrix one, while the degraded material contains much more (uniquely for the totally degraded configuration) porosity. Then for the latter cases the phase contrast between the matrix and the inclusions is more important in average (infinite for totally degraded material), emphasizing the importance of the particle shape (see e.g. [20]).

To assess the influence of the sample volume in the case of the configuration with both spherical and prismatic inclusions, another realization is performed with an edge dimension of the cube of 115 μm. This size leads to increase the sample volume by 52% with respect to the previous 'reference' case. With the same particle size distribution, about 2800 inclusions are necessary to obtain the required volume fractions of hydrated products, porosity and anhydrous residuals. The minimum ratio of sample size over particle dimension is in this case close to 6. The corresponding mesh contains more than 1.15×10^6 nodes and 6.5×10^6 tetrahedral elements; the computations are performed on the same machine type than for the smaller meshes, but they necessitate about twice more time. The results obtained are very close to the ones of the 'reference' case presented in the previous paragraph. When averaged over the three loading directions, the maximum differences are 1.2% for the bulk modulus in case *p*, and 0.7% for the shear modulus in case *td*, with a mean disparity near 0.5% in the degraded cases. It is worth noting that

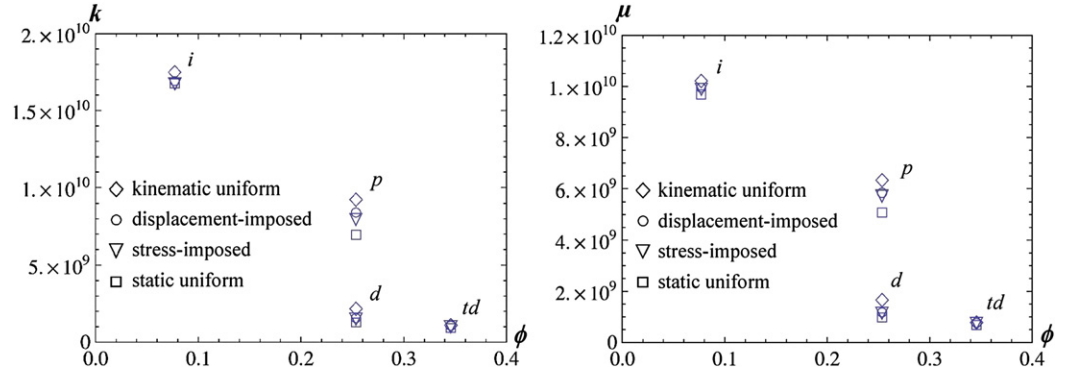

Fig. 6. FE average effective parameters obtained with kinematic (losange) and static (square) uniform boundary conditions, and displacement-imposed (circle) and stress-imposed (triangle) mixed boundary conditions for the microstructure with both spherical and prismatic particles, as a function of the porosity corresponding to the considered degraded states (intact (i), without portlandite (p), same as (p) with degraded C–S–H (d), same as (d) without anhydrous (td)).

Table 3
Overall elastic properties (in GPa) for the two microgeometries in three perpendicular loading directions (displacement mixed boundary conditions).

Configuration	Material state	k_1	k_2	k_3	μ_1	μ_2	μ_3
Spherical and prismatic particles	(i)	16.974	16.964	17.018	10.018	9.978	9.979
	(p)	8.503	8.425	8.514	5.913	5.896	5.861
	(d)	1.645	1.629	1.659	1.238	1.226	1.199
	(td)	1.138	1.129	1.143	0.808	0.789	0.805
Spherical particles	(i)	16.778	16.836	16.761	9.858	9.956	9.931
	(p)	9.468	9.552	9.557	6.228	6.311	6.249
	(d)	1.831	1.862	1.854	1.29	1.333	1.301
	(td)	1.267	1.269	1.276	0.855	0.858	0.857

the moduli are lower for the 'reference' case. For the intact material, the variations are less than 0.1%. Further, the moduli differences between the considered loading directions are at maximum 1.5%, with a mean value around 0.5% in the degraded cases. Due to the small differences between the results obtained on the two microstructures, in the following we assume that the 'reference' sample is large enough to ensure reasonably precise calculations of the apparent elastic moduli.

The FE results obtained with the two types of uniform boundary conditions and the two types of mixed boundary conditions considered in this study are depicted on Fig. 6 for the microstructure with both spherical and prismatic inclusions. As expected from Eq. (12), the effective elastic parameters got with the 3D structure loaded with a prescribed stress (similar to an external pressure applied on the considered face of the RVE) are slightly lower than those gained with displacement-loaded structure in all degradation configurations of the material. The discrepancies are situated between 1% (sound material) and 5% (without portlandite) for the bulk modulus, and between 0.5 and 2% for the shear modulus. The greatest differences are observed for the degraded state without portlandite. Likewise, the static and kinematic uniform boundary conditions provide the lowest and highest elastic moduli, respectively, whatever the configuration. The maximum relative differences are about 40% in the case without portlandite and with degraded C–S–H, whereas they are less than 5% for the intact material. Interestingly, we remark that the results with mixed boundary conditions are situated roughly at equal distance from the upper (kinematic uniform) and lower (static uniform) limits. The differences between the results obtained with the two types of uniform boundary conditions are quite important for the degraded materials, however they are much lower in the case of mixed boundary conditions, even in the degraded states (i.e. for high property contrast). We believe that the latter are sufficiently small to reasonably consider the structures close to RVE. Note that according to [9], the ratio RVE dimension over particle one should be very large (more than 10) in order to get very close numerical results between Dirichlet and Neumann boundary conditions, in particular in the case of high property contrast. Of course more inclusions with smaller sizes compared to the RVE dimensions would be preferable to obtain more reliable and precise results, but this would exceed the memory capacities of our computers.

The macroscopic parameters obtained for the three loading directions (on three different faces) are listed in Table 3 for each degradation state and the two reference particle distributions in the case of displacement-imposed mixed boundary conditions. The differences do not exceed 0.5–1% except for the shear modulus in the degradation state (d) where the variations attain 3%. Note again that the larger discrepancies are observed for the most degraded states, which exhibit the higher phase contrast. Note also that these results are nearly the same for the other loading cases. Once more, owing to the low moduli differences in the perpendicular loading directions, from the viewpoint of isotropy we may reasonably consider that the two generated heterogeneous structures are close to RVE.

Finally, Fig. 7 illustrates the results obtained with the two numerical models in the case of the stress-imposed boundary conditions and the degradation case (d), i.e. without portlandite and degraded C–S–H phase. Fig. 7(a) depicts the displacement on the deformed mesh containing both spherical and prismatic inclusions along the direction **z** when a pressure is applied on the top face of the structure (loading corresponding to the case of Fig. 4 left for the estimation of the bulk modulus), while Fig. 7(b) shows the displacement along the direction **x** on the deformed mesh with only spherical particles when a shear stress is applied in the same direction on the top face of the structure (loading related to the case of Fig. 4 right for the estimation of the shear modulus). As expected, we remark that the displacement field (and then the strains) is not homogeneous on the faces of the structures which are loaded by

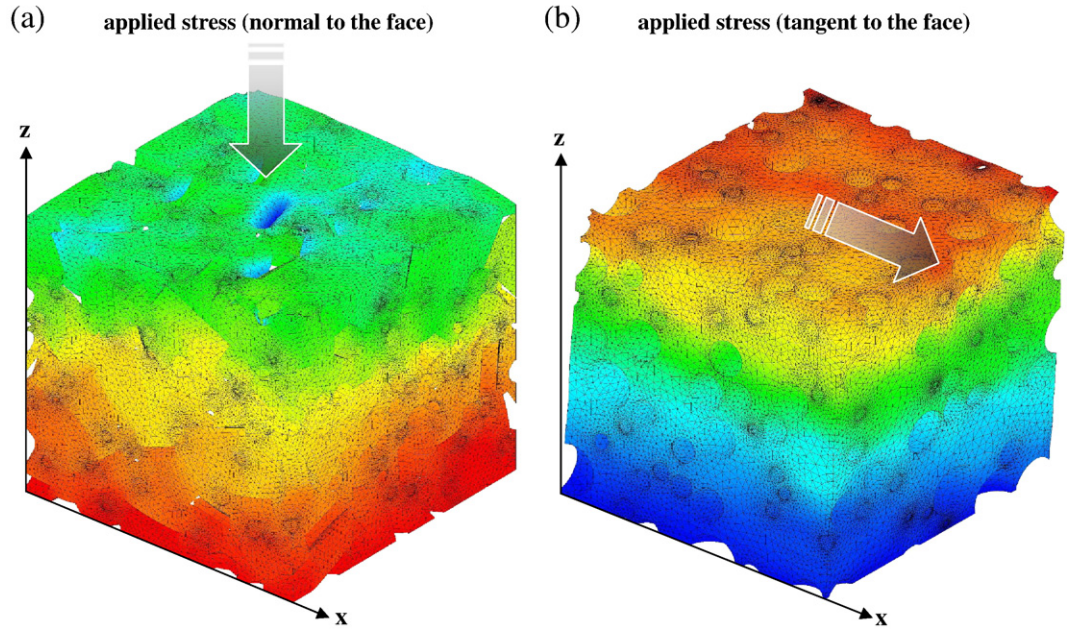

Fig. 7. Illustration of the FE simulations in the case of the stress boundary conditions: displacement along **z** for a pressure applied on the top face of the mesh with both spherical and prismatic inclusions (a) and displacement along **x** for a stress applied in the direction **x** on the top face of the mesh with spherical inclusions (b).

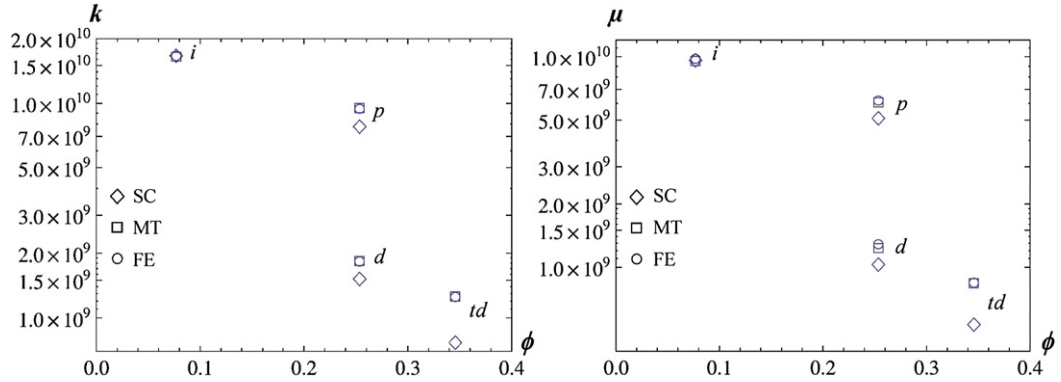

Fig. 8. Effective parameters obtained for the microstructure with only spherical particles with finite element results (FE, displacement-imposed mixed boundary conditions) and with self-consistent (SC) and Mori–Tanaka (MT) schemes as a function of the porosity corresponding to the considered degraded states (intact (i), without portlandite (p), same as (p) with degraded C–S–H (d), same as (d) without anhydrous (td)).

stresses, in particular around the heterogeneities (inclusions and holes materializing porosity and dissolved hydrates).

4. Comparison between analytical and FE results

We compare in this section the performances of the analytical approximation methods briefly recalled in Section 2 to the FE results obtained in the previous section regarding the two generated microstructures. As one of the latter contains only spherical particles while the other includes both spherical and prismatic ones, each analytical scheme is applied twice: a first estimation is performed with only spherical particles and a second with both spherical and ellipsoidal inclusions. Given the shapes of the particles represented in Fig. 2, two different ellipsoids are introduced in this second calculation: one has a prolate form with an aspect ratio of 2 and represents the elongated prisms of Fig. 2(a) and (b) whereas the other exhibits an oblate shape with an aspect ratio of 0.3 for reproducing the platelet-like inclusion of Fig. 2(c).

The FE and analytical results are compared on Figs. 8 and 9 for the two microstructure configurations and the two elastic moduli. The FE results are those obtained with the displacement-imposed mixed boundary conditions (see Fig. 6). The latter are preferred since displacement boundary conditions provide better elastic moduli estimates than stress boundary conditions for the cases where the matrix is stiffer than the inclusive phases, as reported in [9] (this result is opposite when the matrix is more compliant). As for degraded materials the porosity is the main particulate phase, in most cases the matrix is stiffer 'on average' than inclusions. Moreover, we expect that the mixed boundary condition results are closer in general to real RVE macroscopic parameters than those obtained with uniform boundary conditions, the former always being situated between the latter which constitute theoretical upper and lower limits of these macroscopic parameters. Quite unexpectedly, it is clear from these figures that the estimations provided by the approximation schemes are very close to the corresponding FE simulations whatever the degradation states considered, except for the self-consistent scheme which performs comparatively rather poorly. This last point is not surprising since the SC method is more adapted to morphologies in which neither of the phases is privileged, i.e. microstructures resembling to random assemblages of polycrystals, while in the MT and IDD schemes the matrix phase constitutes the reference component in which inclusive phases are dispersed. As the morphology of the studied material is clearly of the matrix-inclusion type, it is natural that the estimation procedures fitting at best the numerical results are those which are established based on a similar microstructure description. Interestingly, some references report that the MT scheme should not be used in the case of composite materials containing more than 20–30% of volume fraction of inclusion (see e.g. [22]), though in the present study this concentration exceeds 35%. While the good performance of these explicit analytical methods may be explained in the sound case by the fact that the matrix phase properties lie between the ones of the diverse inclusive phases (more compliant than anhydrous phase and portlandite, stiffer than pores), thus compensating their higher/lower respective phase contrasts, it is quite surprising to observe that these schemes provide relatively precise estimates even in the case of totally degraded material where the property contrast matrix/inclusion is infinite (since all inclusion are pores). Of course these remarks should be tempered by the fact that the FE results are those obtained with displacement-imposed boundary conditions and that the numerical samples are not strictly speaking real RVEs but only approximated ones. However these general comments are

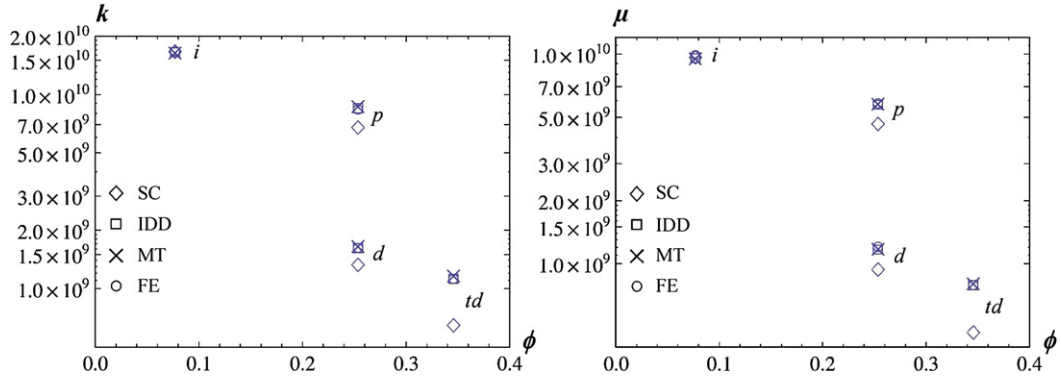

Fig. 9. Effective parameters obtained with finite element results (FE, displacement-imposed mixed boundary conditions) and with self-consistent (SC), Interaction Direct Derivative (IDD) and Mori–Tanaka (MT) schemes for the microstructure with both spherical and prismatic particles, as a function of the porosity corresponding to the considered degraded states (intact (i), without portlandite (p), same as (p) with degraded C–S–H (d), same as (d) without anhydrous (td)).

similar in the case of stress boundary conditions, as both results are very close (see Fig. 6) and lie practically at equal distance between the upper kinematic and lower static uniform boundary conditions.

The differences observed between the two microstructures and illustrated on Fig. 5, in particular in the most degraded cases, seem to be well captured by both MT and IDD schemes, provided the use of ellipsoidal inclusions as defined above. In the case of the structure with only spherical inclusions (Fig. 8), the MT and IDD estimates coincide and the maximum discrepancies between FE and MT-IDD results are less than 2%, whereas they are more than 30% for the SC scheme. In the case of the sample with both spherical and prismatic particles (Fig. 9), MT and IDD predictions diverge slightly especially in the degraded material configurations: the discrepancies reach 4.3% in case *td*, whereas it is only 0.04% in the sound case. When compared to the FE computations obtained with displacement-imposed boundary conditions, the differences are 0.01% and 4.4% in the totally degraded case, 1.7% and 4.2% in the case without portlandite, and 1.6% and 1.7% in the sound case for the IDD and MT schemes, respectively. The IDD method appears then to predict a little better the numerical results; this remark still holds for the mixed stress-imposed boundary conditions. In all situations except for the sound case, the analytical elastic moduli overestimate the numerical ones. Since the FE computed values are slightly lower in the mixed stress boundary conditions case, accordingly the latter differ a little more from the analytical estimates than what is mentioned just above (see Section 3.2).

As in the case of the microstructure with only spherical inclusions, the estimations due to the SC scheme largely underestimate the FE results obtained with both spherical and prismatic particles, except for the non-degraded material. The variations are about 20% in cases *p* and *d*, and reach 40% in the totally degraded case. Again, it appears clearly that the SC scheme is not adapted to the microstructure of the matrix-inclusion type as considered in this study, in particular when at the same time the property contrasts and the volume fraction of the inclusive phases are high. In contrast, the SC method predicts relatively well the elastic moduli of the sound microstructure, which contains inclusive phases with properties lower as well as greater than those of the matrix.

In light of the results presented in this section, we emphasize that the widely used MT scheme and the IDD method give relatively precise estimations of the elastic moduli of microstructure samples exhibiting morphologies of the matrix-inclusion type, as in the case of cementitious materials. These observations seem to be valid even for important volume fraction of particle phase (35% in our case) and for high properties contrast between the matrix and the inclusions (infinite in the totally degraded case). Moreover, these two explicit schemes predict also relatively well the moduli of numerical samples containing non-spherical particles (prismatic in our case) provided that the corresponding inclusions in the analytical methods have ellipsoidal shapes approximating the sample non-spherical ones (the aspect ratios of the ellipsoids have to be suitably determined). Obviously this remark is valid for particle shapes near to ellipsoid; further investigations would be necessary for instance for non-convex and/or more complex shapes. On the opposite, the SC scheme estimates are quite far from the FE results especially for high property contrast between matrix and particulate phases, which is not surprising since by construction this method is more adapted to polycrystalline-like microstructures in which no phase is favoured. Of course these conclusions are suitable for the FE results obtained with displacement-imposed mixed boundary conditions, but they would be nearly the same with the stress-imposed ones since both results are comparable. Finally, we point out that all employed analytical techniques give satisfying prediction of the simulated elastic moduli in the intact material case.

5. Conclusions

We have presented in this paper some numerical results providing the overall mechanical properties of cubic samples representing cementitious materials assumed to be composed of a C–S–H matrix in which are distributed inclusions of different hydrated products (portlandite, ettringite), anhydrous products and porosity. A method has been developed to generate automatically these samples by making use of the functionalities of the numerical platform Salome. This method consists in randomly placing non-overlapping particles of given shapes in a parallelepiped of prescribed dimensions, then in creating a conformant mesh regarding the inclusion geometry with the help of appropriate meshing softwares (BLSURF and GHS3D in our case). Two types of microgeometry were generated, one with only spherical particles and the other with both spherical and prismatic ones, the latter reproducing in a simplified manner the shape of portlandite crystals and ettringite needles. The reference samples contained 850 and 1800 inclusions for the former and latter case, respectively, with a total volume fraction of about 35%. Different situations corresponding to various degradation states of the cementitious material caused by leaching were then simulated in the FE code Cast3M. As the validity of the simulations relies mainly on the hypothesis that the generated microstructures are close to RVEs, verifications of the isotropy condition on these numerical samples were performed by loading them in three perpendicular directions and comparing the corresponding apparent elastic properties. Moreover, two different mixed boundary conditions as well as classical kinematic and static uniform boundary conditions were imposed in order to assess that the samples volume was reasonably high, as it is well known that overall properties calculated on true RVEs are independent of boundary conditions. It was shown the existence of small elastic moduli variations of up to a few percents (about 1–2% on average) between the results obtained with the different loading directions and mixed boundary conditions. Moreover, these mixed boundary condition results were found to be situated just between the upper kinematic and lower static uniform boundary condition calculations. Then, we have assumed that the samples could be reasonably viewed as approximate RVEs. Besides, the influence of the inclusions shape was highlighted through the comparison of computations performed on the two types of microgeometries, where differences in the elastic moduli of more than 10% were reported in the degraded cases. A precise estimation and characterisation of the elastic properties of cementitious materials in various degradation conditions should then carefully integrate such inclusion shape aspects.

The FE numerical results obtained with displacement-imposed mixed boundary conditions were then compared to some of the most widely used effective medium approximation schemes (MT, SC and IDD schemes). Globally, all the models provide good approximations of the sample apparent moduli in the sound case, when the elastic properties of the matrix are situated between those of the particulate phases (i.e. some inclusion are stiffer than the matrix material whereas others are more compliant). However, when the property contrast between the matrix and inclusive phases is high, the SC scheme largely diverges from the FE simulated results while the explicit MT and IDD methods perform quite unexpectedly well. Moreover, the differences of elastic moduli in the leached cases appearing between the two microgeometries, i.e. with only spherical particles and with both spherical and prismatic ones, are remarkably well captured by the latter analytical models providing the approximation of the prismatic particle shapes by ellipsoidal shapes with equivalent aspect ratio. This study then emphasises the fact that the simple explicit analytical models may correctly estimate the effective mechanical parameters of composite media in which particles of various ‘elementary’ shapes are distributed in a matrix, even for relatively high inclusive volume fractions (35%) and high contrast (when inclusions are voids). In our work, computational (obtained with mixed displacement boundary conditions) and analytical elastic moduli differ from less than about 2% in all cases.

The next stage of this study will consist in developing and improving the numerical method generating meshed samples of cementitious materials in order to resemble more the real ones. In particular, it would be of great interest to integrate a hydration model in order to get more precise and realistic arrangements and shapes of

Fig. 10. View of three perpendicular sections of a sample containing about 2800 inclusions.

the particulate phases, instead of a random placement of the inclusions having pre-definite shape. To illustrate this point, Fig. 10 shows three perpendicular faces of the sample with edge dimension of 115 µm, including the intersections of the diverse inclusive phases with the matrix. The proposed enhancement then would lead to render such depictions in reasonable agreement with sections obtained experimentally for instance by image analysis techniques.

Acknowledgment

The authors are grateful to P. Verpeaux (CEA, DEN, DM2S, LM2S) for his help in improving the software Cast3m regarding the computations of large systems.

References

[1] J.D. Eshelby, The determination of the elastic field of an ellipsoidal inclusion, and related problems, Proceedings of the Royal Society of London Series A-Mathematical and Physical Sciences, vol. 241(1226), 1957, pp. 376–396.
[2] T. Mori, K. Tanaka, Average stress in matrix and average elastic energy of materials with misfitting inclusions, Acta Metall. 21 (5) (1973) 571–574.
[3] Y. Benveniste, A new approach to the application of Mori–Tanaka's theory in composite materials, Mech. Mater. 6 (2) (1987) 147–157.
[4] D.A.G. Bruggeman, Berechnung verschiedener physikalischer Konstanten von heterogenen Substanzen. I. Dielektrizitätskonstanten und Leitfähigkeiten der Mischkörper aus isotropen Substanzen, Annalen der Physik 416 (7) (1935) 636–679.
[5] R. Landauer, The electrical resistance of binary metallic mixtures, J. Appl. Phys. 23 (7) (1952) 779–784.
[6] R. Hill, A self-consistent mechanics of composite materials, J. Mech. Phys. Solids 13 (4) (1965) 213–222.
[7] Z. Hashin, S. Shtrikman, A variational approach to the theory of the elastic behaviour of multiphase materials, J. Mech. Phys. Solids 11 (2) (1963) 127–140.
[8] T. Kanit, S. Forest, I. Galliet, V. Mounoury, D. Jeulin, Determination of the size of the representative volume element for random composites: statistical and numerical approach, Int. J. Solids Struct. 40 (13–14) (2003) 3647–3679.
[9] S. Pecullan, L.V. Gibiansky, S. Torquato, Scale effects on the elastic behavior of periodic and hierarchical two-dimensional composites, J. Mech. Phys. Solids 47 (7) (1999) 1509–1542.
[10] W.J. Drugan, J.R. Willis, A micromechanics-based nonlocal constitutive equation and estimates of representative volume element size for elastic composites, J. Mech. Phys. Solids 44 (4) (1996) 497–524.
[11] A.A. Gusev, Representative volume element size for elastic composites: a numerical study, J. Mech. Phys. Solids 45 (9) (1997) 1449–1459.
[12] S. Bishnoi, K.L. Scrivener, Numerical experimentation with cement using µic, International RILEM Symposium on Concrete Modelling – CONMOD'08, Delft, The Netherlands, 2008 369–378.
[13] D.P. Bentz, Three-dimensional computer simulation of portland cement hydration and microstructure development, J. Am. Ceram. Soc. 80 (1) (1997) 3–21.
[14] S. Béjaoui, B. Bary, S. Nitsche, D. Chaudanson, C. Blanc, Experimental and modeling studies of the link between microstructure and effective diffusivity of cement pastes, Revue Européenne de Génie Civil 10 (9) (2006) 1073–1106.
[15] F. Bernard, S. Kamali-Bemard, W. Prince, 3D multi-scale modelling of mechanical behaviour of sound and leached mortar, Cem. Concr. Res. 38 (4) (2008) 449–458.
[16] N. Sukumar, D.L. Chopp, N. Moes, T. Belytschko, Modeling holes and inclusions by level sets in the extended finite-element method, Comput. Meth. Appl. Mech. Eng. 190 (46–47) (2001) 6183–6200.
[17] J. Yvonnet, H. Le Quang, Q.C. He, An XFEM/level set approach to modelling surface/interface effects and to computing the size-dependent effective properties of nanocomposites, Comput. Mech. 42 (1) (2008) 119–131.
[18] I.G. Richardson, The nature of the hydration products in hardened cement pastes, Cem. Concr. Compos. 22 (2) (2000) 97–113.
[19] T.T. Wu, The effect of inclusion shape on the elastic moduli of a two-phase material, Int. J. Solids Struct. 2 (1) (1966) 1–8.
[20] E. Stora, Q.C. He, B. Bary, Influence of inclusion shapes on the effective linear elastic properties of hardened cement pastes, Cem. Concr. Res. 36 (7) (2006) 1330–1344.
[21] Q.S. Zheng, D.X. Du, An explicit and universally applicable estimate for the effective properties of multiphase composites which accounts for inclusion distribution, J. Mech. Phys. Solids 49 (11) (2001) 2765–2788.
[22] S. Torquato, Random Heterogeneous Media: Microstructure and Macroscopic Properties, Springer-Verlag, New York, 2001.
[23] P. Ponte Castaneda, J.R. Willis, The effect of spatial distribution on the effective behavior of composite materials and cracked media, J. Mech. Phys. Solids 43 (12) (1995) 1919–1951.
[24] B. Bary, Estimation of mechanical and transfer parameters in unsaturated isotropic microcracked concrete, Submitted for publication (2009).
[25] T. Mura, Micromechanics of Defects in Solids, Martinus Nijhoff, The Hague, 1982.
[26] B. Budiansky, On the elastic moduli of some heterogeneous materials, J. Mech. Phys. Solids 13 (1965) 223–227.
[27] www.salome-platform.org.
[28] K.L. Scrivener, Backscattered electron imaging of cementitious microstructures: understanding and quantification, Cem. Concr. Compos. 26 (8) (2004) 935–945.
[29] K. Sab, On the homogenization and the simulation of random materials, Eur. J. Mech. A-Solids 11 (5) (1992) 585–607.
[30] C. Huet, Application of variational concepts to size effects in elastic heterogeneous bodies, J. Mech. Phys. Solids 38 (6) (1990) 813–841.
[31] S. Hazanov, C. Huet, Order relationships for boundary conditions effect in heterogeneous bodies smaller than the representative volume, J. Mech. Phys. Solids 42 (12) (1994) 1995–2011.
[32] C.J. Haecker, E.J. Garboczi, J.W. Bullard, R.B. Bohn, Z. Sun, S.P. Shah, T. Voigt, Modeling the linear elastic properties of portland cement paste, Cem. Concr. Res. 35 (10) (2005) 1948–1960.
[33] G. Constantinides, F.-J. Ulm, The effect of two types of C–S–H on the elasticity of cement-based materials: results from nanoindentation and micromechanical modeling, Cem. Concr. Res. 34 (1) (2004) 67–80.